coordinate, and the vertical velocity U_v is estimated from continuity as $U_h h \approx U_v L$. Then, $\mathrm{d}L_{crystal}/\mathrm{d}t \approx 2 \times 10^{-7}\,\mathrm{m\,s^{-1}}$, which is consistent with the appearance of crystallites observable to the eye only after days. So the buoyancy-driven instability of the fluid in the temperature gradient establishes a convective flow that carries PMMA particles from the hot end to the cool end. The flux of particles deposits some at the cool end due to the low chemical potential of the solid that forms there. A diffusional boundary layer feeds the nucleation and growth process. This crystallization is controlled by the flux of particles along the volume fraction gradient, and can produce very large hard-sphere single crystals if the volume fraction at the cool end is maintained near 0.50 and few nuclei are produced initially.

Moving the heater also has interesting effects. If the velocity is slightly faster than the motion of the growing liquid–solid interface, we observe a more diffuse interface (Fig. 4a), as well as the dendritic growth instability normally found for samples in the coexistence region (Fig. 4b).

We have demonstrated the ability to manipulate the motion of spheres in a suspension using temperature gradients. In the presence of gravity, the convective flow provides the mechanism for macroscopic transport of the particles. The diffusion regime at the cool end of the temperature gradient provides a zone for controlled nucleation and growth of hard-sphere crystals. In the absence of gravity, diffusion fields could be used to control volume fraction more directly in smaller cells. There are other possible uses of temperature gradients. Temperature gradients combined with the colloidal epitaxy technique should allow controlled growth of oriented single crystals. Moving a high-temperature region through a crystalline sample should sweep a low-volume-fraction liquid band through the solid in a technique similar to zone refining for conventional crystals. □

1. Joannopoulos, J. D., Villeneuve, P. R. & Fan, S. Photonic crystals: putting a new twist on light. *Nature* **386**, 143–149 (1997).
2. Pan, G., Kesavamoorthy, R. & Asher, S. A. Optically nonlinear Bragg diffracting nanosecond optical switches. *Phys. Rev. Lett.* **78**, 3860–3863 (1997).
3. Holtz, J. H. & Asher, S. A. Polymerized colloidal crystal hydrogel films as intelligent chemical sensing materials. *Nature* **389**, 829–832 (1997).
4. Pusey, P. N. & van Megen, W. Phase behavior of concentrated suspensions of nearly hard colloidal spheres. *Nature* **320**, 340–342 (1986).
5. Pusey, P. N. in *Liquids, Freezing and the Glass Transition* Ch. 10 (eds Hansen, J. P., Levesque, D. & Zinn-Justin, J.) 763–942 (Elsevier, Amsterdam, 1991).
6. Poon, W. C. K. & Pusey, P. N. in *Observation, Prediction and Simulation of Phase Transitions in Complex Fluids* (eds Baus, M., Rull, L. F. & Ryckaert, J. P.) 3–51 (Kluwer Academic, Boston, 1995).
7. Dinsmore, A. D., Crocker, J. C. & Yodh, A. G. Self-assembly of colloidal crystals. *Curr. Opin. Colloid Interface Sci.* **3**, 5–11 (1998).
8. Grier, D. G. (ed.) From dynamics to device: directed self-assembly of colloidal materials. *MRS Bull.* **23** (10), 21–50 (1998).
9. van Blaaderen, A., Ruel, R. & Wiltzius, P. Template-directed colloidal crystallization. *Nature* **385**, 321–324 (1997).
10. Zhu, J. *et al.* Crystallization of hard-sphere colloids in microgravity. *Nature* **387**, 883–885 (1997).
11. Cheng, Z. *Colloidal Hard Sphere Crystallization and Glass Transition.* Thesis, Princeton Univ. (1998).
12. Hoover, E. G. & Ree, F. H. Melting transition and communal entropy for hard spheres. *J. Chem. Phys.* **49**, 3609–3617 (1968).
13. Woodcock, L. V. Glass transition in the hard sphere model and Kauzmann's paradox. *Ann. NY Acad. Sci.* **371**, 274–298 (1981).
14. Phan, S.-E. *et al.* Phase transition, equation of state, and limiting shear viscosities of hard sphere dispersions. *Phys. Rev. E* **54**, 6633–6645 (1996).
15. Underwood, S. M., Taylor, J. R. & van Megen, W. Sterically stabilized colloidal particles as model hard spheres. *Langmuir* **10**, 3550–3554 (1994).
16. Woodcock, L. V. Entropy difference between the face-centred cubic and hexagonal close-packed crystal structures. *Nature* **385**, 141–143 (1997).
17. Bolhuis, P. G. *et al.* Entropy difference between crystal phases. *Nature* **388**, 235–236 (1997).
18. Pronk, S. & Frenkel, D. Can stacking faults in hard-sphere crystals anneal out spontaneously? *J. Chem. Phys.* **110**, 4589–4592 (1999).
19. Mau, S-C. & Huse, D. A. Stacking entropy of hard-sphere crystals. *Phys. Rev. E* **59**, 4396–4401 (1999).
20. Pusey, P. N. *et al.* Structure of crystals of hard colloidal spheres. *Phys. Rev. Lett.* **63**, 2753–2756 (1989).
21. Russel, W. B. *et al.* Dendritic growth of hard sphere crystals. *Langmuir* **13**, 3871–3881 (1997).
22. He, Y., Olivier, B. & Ackerson, B. J. Morphology of crystals made of hard spheres. *Langmuir* **13**, 1408–1412 (1997).
23. Hurd, A. J. *et al.* Lattice dynamics of colloidal crystals. *Phys. Rev. A* **26**, 2869–2881 (1982).
24. Derksen, J. & Van de Water, W. Hydrodynamics of colloidal crystals. *Phys. Rev. A* **45**, 5660–5673 (1992).
25. Pradhan, R. D. *et al.* Photonic band structure of bcc colloidal crystals. *Phys. Rev. B* **55**, 9503–9507 (1997).
26. Tarhan, I. I. & Watson, G. H. Photonic band structure of fcc colloidal crystals. *Phys. Rev. Lett.* **76**, 315–318 (1996).
27. Carnahan, N. F. & Starling, K. E. Equation of state for nonattracting rigid sphere. *J. Chem. Phys.* **51**, 635–636 (1969).
28. Hall, K. R. Another hard-sphere equation of state. *J. Chem. Phys.* **57**, 2252–2254 (1972).
29. Guinier, A. *X-ray Diffraction* (Freeman, San Francisco, 1963).
30. Sanders, J. V. Diffraction of light by opals. *Acta Crystallogr. A* **24**, 427–434 (1968).

··

High-efficiency multilevel zone plates for keV X-rays

E. Di Fabrizio*, **F. Romanato***, **M. Gentili**†, **S Cabrini**†, **B. Kaulich**‡, **J. Susini**‡ & **R. Barrett**‡

* *TASC-INFM (National Institute for the Physics of Matter), Elettra Synchrotron Light Source, Lilit Beam-line SS14 km 163.5, Area Science Park, 34012 Basovizza, Trieste, Italy*
† *Istituto di Elettronica dello Stato Solido, Via Cineto Romano 42, 00156 Rome, Italy*
‡ *X-Ray Microscopy Beamline, European Synchrotron Radiation Facility, BP220, F-38043 Grenoble Cedex, France*

·· ·· ··

The development of high brilliance X-ray sources coupled with advances in manufacturing technologies has led to significant improvements in submicrometre probes for spectroscopy, diffraction and imaging applications. The generation of a small beam spot size is commonly based on three principles[1]: total reflection (as used in optical elements involving mirrors or capillaries), refraction (such as in refractive lenses[2]) and diffraction. The latter effect is employed in Bragg–Fresnel or Soret lenses, commonly known as Fresnel zone plate lenses. These lenses currently give the best spatial resolution, but are traditionally limited to rather soft X-rays—at high energies, their use is still limited by their efficiency. Here we report the fabrication of high-efficiency, high-contrast gold and nickel multistep (quaternary) Fresnel zone plates using electron beam lithography. We achieve a maximum efficiency of 55% for the nickel plate at 7 keV. In addition to their high efficiency, the lenses offer the advantages of low background signal and effective reduction of unwanted diffraction orders. We anticipate that these lenses should have a significant impact on techniques such as microscopy[3], micro-fluorescence[4] and micro-diffraction[5], which require medium resolution (500–100 nm) and high flux at fixed energies.

It is only in the last decade, almost a century after the discovery of X-rays (by Röntgen, in 1895), that optical elements with good efficiency and submicrometre resolution have become available. The delays in fabricating such optics were due to the difficulty of realising refraction and reflection at X-ray wavelengths. The physical origin of this technical difficulty is closely linked to the real, phase-shifting part of the refractive index that, for all materials at X-ray wavelengths, is very close to unity (that is, the contrast with respect to the vacuum is very small).

The progress achieved in micro-fabrication has stimulated interest in the fabrication of diffractive optics and, in particular, Fresnel zone plates (FZPs)[6] (Fig. 1). Many studies considered FZPs to be promising optical elements for microscopy and microprobe applications[1–18]. This work is related to the development of phase FZP

with 20–40% efficiency in the 5–8 keV energy range[7–9], at the Advanced Photon Source at Argonne National Laboratory.

A circular multilevel FZP[10] (Fig. 2) is a good approximation[11] of an ideal continuous phase-shifting profile (that is, kinoform) and consists of a series of concentric zone rings, whose radius $r_{n,L}$ is determined by:

$$r_{n,L} = \sqrt{\lambda f \left(2\frac{l}{L} + n - 2 \right)} \qquad (1)$$

where λ is the wavelength, f is the focal length and n is the zone index number (in equation (1), n may have only even values). Each zone is divided into L levels whose index is $l \leq l \leq L$. For a binary FZP ($L = 2$), the zone radius law reduces to the well known binary FZP relation[10], $r_{n,2} = \sqrt{\lambda f n}$. The optical resolution of an FZP is given by $\delta_m = 1.22\Delta r_{N,L}/m$, where δ_m is the FWHM (full-width at half-maximum) of the Airy disk (the central maximum of the diffraction pattern from a circular lens) at the focal plane for the mth diffraction order, N is the outermost zone index and $\Delta r_{N,L}$ is the outermost zone width. Figure 2 illustrates the working principle of a quaternary FZP ($L = 4$).

The total radiation amplitude delivered by the FZP to the focus can be calculated by using the phasor method[12]. The phase shifter of thickness Δt changes the phase by $\phi = 2\pi \Delta t \delta/\lambda$ and attenuates the field amplitude by a factor of $e^{-2\pi\kappa\Delta t/\lambda}$, where δ is the deviation of the real part from unity and κ is the imaginary part of the refractive index, $n_r = 1 - \delta + i\kappa$. When the diffraction condition $\Delta t L \delta = \lambda$ is satisfied, the amplitude A^m is given by:

$$A^m = \frac{C\left[\exp\left(i2\pi\frac{m}{L}\right) - 1\right]}{i2\pi m} \cdot \sum_{l=1}^{L} \exp\left[-2\pi\frac{\kappa}{\delta}\frac{(l-1)}{L}\right]$$
$$\cdot \exp\left[+i2\pi\frac{(l-1)}{L}(m-1)\right] \qquad (2)$$

C is the intensity of the incoming field. The contribution of the diffraction order is taken into account by the index $m = 0, \pm 1, \pm 2\ldots$.

From equation (2) the FZP efficiency can be derived, defined as $\eta^m = |A_p^n|^2/C^2$ for the mth diffraction order. As opposed to the more common binary FZP, the groove asymmetry of the multilevel FZP introduces new phase contributions that interfere in such a way as to concentrate the photon flux in the first diffraction order and to suppress the others almost completely. The imaginary term of the sum in equation (2) accounts for the selection rules of the diffractive order selection. In the limit of zero attenuation ($\kappa = 0$) this term becomes:

$$\sum_{l=1}^{L} \exp\left[+i2\pi\frac{(l-1)}{L}(m-1)\right] = \begin{cases} L & \text{if } (m-1) = 0, \pm L, \pm 2L, \ldots \\ 0 & \text{otherwise} \end{cases}$$
$$(3)$$

The result is that the first order is active and that the other active orders have a periodicity of L. The efficiency is $\eta^m = 2(1 - \cos(2\pi m/L))(L/m)^2$.

When absorption in the zones is considered, the theoretical diffraction efficiency of the first order decreases slightly. For a photon energy of 7 keV, it changes from 81.5% to 72% for a FZP made of nickel and to 55% for a gold FZP. Absorption also allows forbidden orders to appear; however, their intensity remains negligible. The zero-order intensity is higher, but <1%.

On the basis of these results we have fabricated gold (Fig. 1a and b) and nickel (Fig. 1c) FZP lenses for the energy range 5–8 keV. The geometrical characteristics of our FZP at an energy of 8 keV are: focal length, 1 m; diameter, 150 μm; number of levels $L = 4$; outermost zone-width for the fourth level, 500 nm. A polymethyl methacrylate (PMMA) resist, 1.8 μm thick, was patterned by using electron beam lithography at an energy of 50 keV. The

complete multilevel FZP was manufactured by a three-step process consisting of exposure and electroplating deposition of each level. We developed a custom alignment procedure to reach an accuracy better than 50 nm.

The FZP tests were carried out on the X-ray microscopy beam-line ID21 at ESRF[13] (European Synchrotron Radiation Facility), which can operate over an energy range of 2–8 keV. The FZP
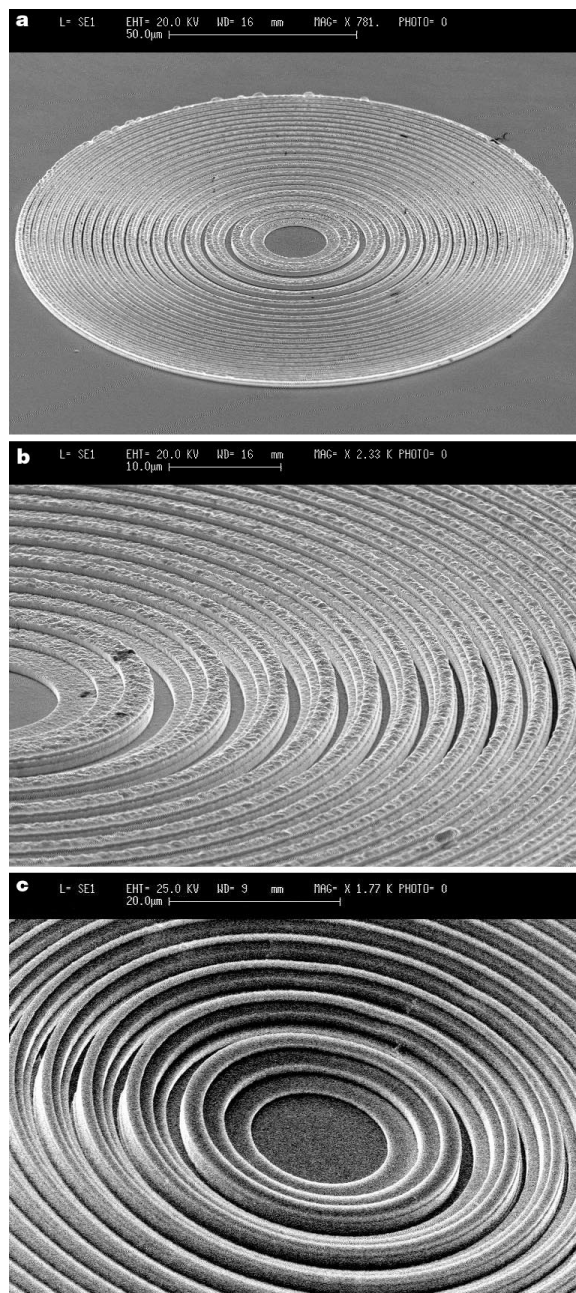

Figure 1 Scanning electron microscope image of quaternary gold (**a**, **b**) and nickel (**c**) Fresnel zone plates. A Fresnel zone plate (FZP) consists of concentric rings designed so that the incident radiation is modulated in amplitude and/or in phase in order to interfere constructively along the optical axis at a point that represents the lens focus. The figure shows FZPs with multilevel profiles. This geometry offers the double advantage of increasing the efficiency (that is, the fraction of the incident intensity delivered to the focus) and of introducing selection rules that highly suppress unwanted diffraction orders. The fabrication of a multilevel FZP requires the deposition and alignment of subsequent levels with an accuracy of a fraction of the desired spatial resolution. The geometrical characteristics designed for 8 keV are: focal length, 1 m; diameter, 150 μm; number of levels, 4; and outermost zone-width of the fourth level, 500 nm. Scale bars: **a**, 50 μm; **b**, 10 μm; **c**, 20 μm.

Table 1 Optical and fabrication design parameters of a quaternary zone plate

Energy (keV)	Theoretical efficiency (%)	Gain	Spot size (nm)	Diameter (mm)	FZP outermost linewidth (nm)	Phase-shifter thickness (µm)
0.76 (low)	40	10^7	100	0.5	50	0.25
7 (medium)	65	10^6	300	0.5	150	1.3
35 (high)	80	10^5	2,000	1	1,000	6.1

efficiency measurements were performed at 5.5, 6.0, 7.0 and 8 keV. The zone plate and the 10 µm pinhole in the focal plane were mutually aligned by means of a stage with a mechanical resolution of 10 nm.

At an energy of 7 keV, the gold FZP provided an efficiency of 38%. The highest efficiency, of 55%, was obtained by the nickel FZP at 7 keV. At 5.5 and 8 keV the efficiency is, however, still higher than 40%. Figure 3a shows the theoretical and experimental efficiency of the nickel FZP. The optical gain (the ratio between the photon density delivered by the FZP at the focus and the photon density impinging on the FZP) is by definition $g = \eta(r_N/(\sigma_x\sigma_y)^{0.5})^2$, where r_N is the FZP diameter and $\sigma_x\sigma_y$ the spot size. The experimental value calculated for the nickel FZP at 7 keV is about 2,500. If we were to work at the diffraction limit by reducing the source size, we would expect a flux gain $g \approx 8,000$. In FZP-based scanning X-ray microscopy, it is common to place an order sorting aperture (OSA) of a few micrometres in the path of the optical axis to decrease the background from spurious orders and thus optimise the image contrast. Figure 3b is a two-dimensional intensity map collected at the focal plane with an OSA with a diameter of 10 µm. The background intensity that passes through an OSA aperture can be written as: $I_{OSA}^{\pm m_L} = K_L I^{\pm m_L}$, where $I^{\pm m_L}$ are the spurious orders ($m_L \neq 1$). The K_L factor is given by:

$$K_L = \left(\frac{r_{OSA}}{r_{ZP}}\right)^2 \sum_{m_L} \frac{1}{(m_L - 1)^2} \qquad (4)$$

Equation (4) shows that the quaternary FZP background intensity passing through the OSA is damped by a factor of 10 compared to binary FZP. Reinforcing the diffracted light for a single order makes the use of an OSA unnecessary, and allows multilevel FZPs to be used in a similar way to standard optical lenses. This could be a major advantage in some practical cases in which the conventional geometry (such as the sample–OSA distance) limits the sample environment.

Quaternary FZP can also be used as lenses to condense the beam in an imaging transmission X-ray microscope which requires high flux to be delivered onto the sample with low background. However, within the keV energy range, quaternary FZPs have to be used in conjunction with an additional optical component which allows the numerical aperture of the whole condenser to be matched with the numerical aperture of the X-ray objective lens[14].

To further assess the potential of a quaternary FZP, we discuss the most relevant fabrication parameters: (1) the spatial resolution (the minimum line-width attainable), (2) the aspect ratio (the ratio between the height and the width of a structure), and (3) the alignment between levels. These fabrication figures of merit are
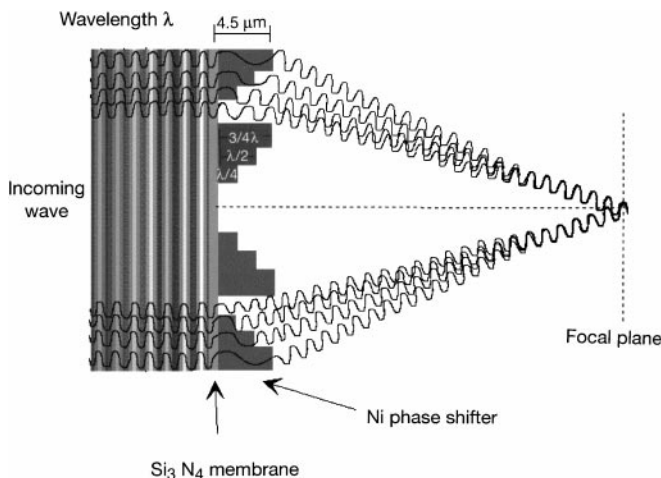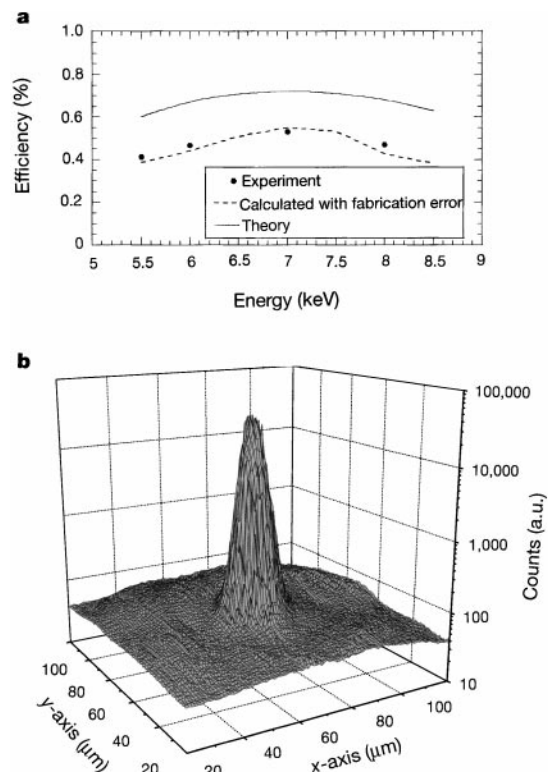

Figure 2 The working principle of a quaternary Fresnel zone plate. The FZP can be based either on amplitude or phase-shift modulation. In the former case, the FZP is necessarily binary. The light impinging on the zones with alternate index is suppressed, by absorption, in such a way that only the wave passing through the open zones will interfere constructively at the focus point. The efficiency of an amplitude FZP cannot be higher than 10%. In the case of phase-shift FZPs, instead of suppressing the part of the incident radiation with the wrong phase, diffraction is performed by phase modulation and allows a binary phase-shift FZP to have an efficiency of up to 40%. In multilevel phase-shift FZPs, diffraction is performed by phase modulation. The FZP described by equation (1) has a periodicity of $2\lambda f$ in r^2 coordinates. This means that over a period ($\Delta n = 2$) the optical path of the incident radiation increases by λ and the phase by 2π. Within each zone, the level zones represent the interval ($\Delta l = 1$) where the phase of the incident radiation increases by $2\pi/L$. For each level zone, an appropriate thickness of the refractive material (phase-shifter) is then added to the different X-ray optical paths to correct this phase difference. The FZP is fabricated on a Si_3N_4 membrane 2 µm thick.

Figure 3 Efficiency and intensity of map of the nickel FZP. **a**, Theoretical and experimental efficiency of a FZP versus energy for the quaternary nickel zone plate. The difference is attributed to fabrication errors, such as electroplating growth, line-width errors and alignment errors. **b**, Two-dimensional intensity map collected at the focal plane through an order sorting aperture with a diameter of 10 µm. The background level is noticeably low compared to the peak intensity (the z axis is a logarithmic scale). This result is due to the multilevel geometry that strongly reduces the intensity in the spurious diffraction orders, and reinforces the first-order peak by a factor of 680 compared to the other orders. a.u., arbitrary units.

related to the optical performances and to the energy at which the optical device is designed to work. In Table 1, the energy region from 500 eV to 50 keV is divided into three parts: low, medium and high energies.

At low energies, the material thickness needed to provide a π-phase shift becomes smaller (200–300 nm), but it is still necessary to achieve high aspect ratios of about 10 if one wishes to fabricate zones at the current lithographic spatial resolution limit[15,16]. With the latest generation of electron-beam machines and nano-structuring technologies[17,18], zone plates with a resolution of 20–50 nm have been fabricated for 200–500 eV X-rays, and alignment accuracy of ~10 nm has already been demonstrated[8]. Working at the lithographic limit, the outermost zone width of a quaternary FZP becomes twice as large as that of a binary FZP, thus doubling the optical resolution $\delta_{r,m}$. Therefore, at low energy, quaternary FZPs are complementary to binary FZPs, providing a good trade-off between the reduction of the optical resolution and the increase of the efficiency.

At medium energy, the typical phase-shifter thickness is of the order of one micrometre. Practical aspect ratios of 5–10, that can be achieved by today's very-large-scale integration (VLSI) technology, limit the minimum spatial resolution to 150 nm. At high energy, the phase-shifter thickness further increases to a few micrometres (see Table 1) and, accordingly, the minimum feature size reaches about 1 μm. In this range, where other optical devices are somewhat limited (although refractive lenses could improve in the future), quaternary FZPs show some unique advantages, especially with respect to their efficiency and optical resolution (see Table 1). Also, multilevel FZPs are compatible at high energy with microdiffraction, where the high focusing length matches the necessary low angular divergence.

With the consolidation of third-generation synchrotrons, multilevel FZPs could be used as focusing elements in research fields where high efficiency and high signal-to-noise ratio are needed at X-ray wavelengths. □

1. Dhez, P., Chevallier, P., Lucatorto, T. B. & Tarrio, C. Instrumental aspects of X-ray microbeams in the range above 1 keV. *Rev. Sci. Instrum.* **70**, 1907–1920 (1999).
2. Snigirev, A., Kohn, V., Snigireva, I. & Lengeler, B. A compound refractive lens for focusing high-energy X-rays. *Nature* **384**, 49–51 (1996).
3. Kirz, J., Jacobsen, C. & Howells, M. Soft X-ray microscopes and their biological applications. *Q. Rev. Biophys.* **28**, 33–130 (1995).
4. Wang, J. *et al.* X-ray fluorescence correlation spectroscopy: a method for studying particle dynamics in condensed matter. *Phys. Rev. Lett.* **80**, 1110–1113 (1998).
5. Rodrigues, W. *et al.* X-ray microdiffraction studies of an integrated laser-modulator system in *Proc. 6th Conf. on Synchrotron Radiation Instrumentation (SRI97)* (Himeji Citizen Hall, Hyogo, Japan, 1997).
6. Tatchyn, R. O. in *X-ray Microscopy* Vol. 43 (eds Smah, G. & Rudolph, D.) 40–50 (Springer Series in Optical Sciences, Springer, Berlin, 1990).
7. Lai, B. *et al.* Hard X-ray phase zone plate fabricated by Lithographic techniques. *Appl. Phys. Lett.* **1**, 1877–1880 (1992).
8. Di Fabrizio, E. *et al.* High-performance multilevel blazed X-ray microscopy Fresnel zone plates fabricating using X-ray lithography. *J. Vac. Sci. Technol. B.* **12**, 3979 (1994).
9. Yun, W. *et al.* Nanometer focusing of hard X-rays by phase zone plates. *Rev. Sci. Instrum.* **70**, 2238–2241 (1999).
10. Michette, A. G. *Optical Systems for Soft X-rays* (Plenum, New York, 1986).
11. Schelokob, I. A. *et al.* Second generation of grazing-incidence-phase Fresnel zone plates. *Opt. Commun.* **159**, 278–284 (1999).
12. Kirz, J. Phase zone plates for X-rays and extreme UV. *J. Opt. Soc. Am.* **64**, 301–309 (1974).
13. Barrett, R., Kaulich, B., Oestreich, S. & Susini, J. The scanning microscopy end-station at the ESRF X-ray microscopy beamline. *Proc. SPIE* **3499**, 80–90 (1998).
14. Nieman, B. in *X-ray Microscopy and Spectromicroscopy* (eds Thieme, J., Schmahl, G., Rudolph, D. & Umbach, E.) 44–55 (Springer, Chernogolovka, Russia, 1998).
15. Spector, S. J., Jaconsen, C. J. & Tennant, D. M. Process optimization for production of sub-20 nm soft X-ray zone plate. *J. Vac. Sci. Technol. B* **15**, 2872–2876 (1997).
16. David, C. *et al.* Low-distortion electron-beam lithography for fabrication of high-resolution germanium and tantalum phase zone plates. *J. Vac. Sci. Technol. B* **13**, 2762–2766 (1995).
17. Schneider, G., Schliebe, T. & Aschoff, H. Cross linked polymers for nanofabrication of high resolution zone-plates in nickel and germanium. *J. Vac. Sci. Technol. B* **13**, 2809–2812 (1995).
18. Weiss, D., Peuker, M. & Schneider, G. Radiation enhanced network formation in copolymer galvanoforms for diffractive nickel X-ray optics with high aspect ratios. *Appl. Phys. Lett.* **72**, 1805–1807 (1998).

Influence of environmental changes on degradation of chiral pollutants in soils

David L. Lewis*†, A. Wayne Garrison*, K. Eric Wommack*†, Alton Whittemore*, Paul Steudler‡ & Jerry Melillo‡

* US Environmental Protection Agency, Ecosystems Research Division, National Exposure Research Laboratory, Athens, Georgia 30605, USA
† Department of Marine Sciences, University of Georgia, Athens, Georgia 30602, USA
‡ The Ecosystems Center, Marine Biological Laboratory, Woods Hole, Massachusetts 02542, USA

....

Numerous anthropogenic chemicals of environmental concern— including some phenoxy acid herbicides, organophosphorus insecticides, polychlorinated biphenyls, phthalates, freon substitutes and some DDT derivatives—are chiral. Their potential biological effects, such as toxicity, mutagenicity, carcinogenicity, and endocrine disrupter activity, are generally enantiomer-selective, and different enantiomers are preferentially degraded (transformed) by micro-organisms in various environments[1–8]. Here we use field and laboratory experiments to demonstrate that environmental changes in soils can alter these preferences, and to suggest that the preferences shift owing to different groups of related microbial genotypes being activated by different environmental changes. In Brazilian soils, almost all pasture samples preferentially transformed the non-herbicidal enantiomer of dichlorprop ((RS)-2-(2,4-dichlorophenoxy)propionic acid), while most forest samples either transformed the herbicidal enantiomer more readily or as rapidly as the non-herbicidal enantiomer. Organic nutrient enrichments shifted enantioselectivity for methyl dichlorprop ((RS)-methyl 2-(2,4-dichlorophenoxy)propionic acid) strongly towards preferentially removing the non-herbicidal enantiomer in soils from Brazil and North America, potentially increasing phytotoxicity of its residues relative to that of the racemate. Assessments of the risks chemical pollutants pose to public health and the environment need to take into account the chiral selectivity of microbial transformation processes and their alteration by environmental changes, especially for pesticides as up to 25 per cent are chiral[9].

Enantiospecific biological effects associated with chiral chemicals are well recognized in the pharmaceutical industry where 50 of the top 100 most widely sold drugs, including barbiturates, ibuprofen, albuterol, and Ritalin, are marketed as single enantiomers to avoid adverse side effects[8,10]. The high cost of separating enantiomers
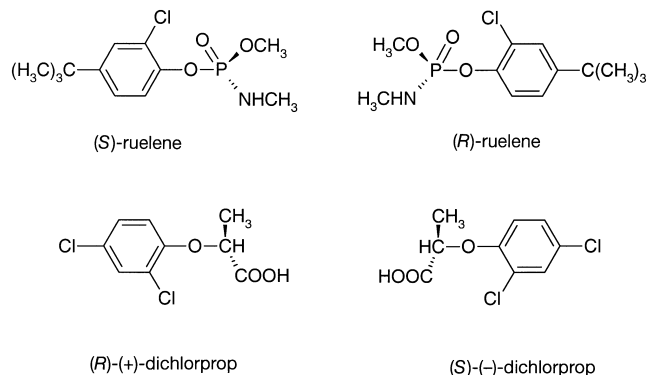

Figure 1 Enantiomers of ruelene and dichlorprop.